ISSN 1674-1056
http://cpb.iphy.ac.cn
http://iopscience.iop.org/cpb
中国物理 B
Chinese Physics
中国物理
Chinese Physics B

Reconstruction model for temperature and concentration profiles ofsoot and metal-oxide nanoparticles in a nanofluid fuel flameby using a CCD camera

Guannan Liu(刘冠楠), Dong Liu(刘冬)
Citation: Chin. Phys. B . 2018, 27(5): 054401. **doi:** 10.1088/1674-1056/27/5/054401

Journal homepage: http://cpb.iphy.ac.cn; http://iopscience.iop.org/cpb

What follows is a list of articles you may be interested in

Two-dimensional thermal illusion device with arbitrary shape based on complementary media

Ge Xia(夏舸), Wei Kou(寇蔚), Li Yang(杨立), Yong-Cheng Du(杜永成)
Chin. Phys. B . 2017, 26(10): 104403. **doi:** 10.1088/1674-1056/26/10/104403

Simulation on effect of metal/graphene hybrid transparent electrode on characteristics of GaN light emitting diodes

Ming-Can Qian(钱明灿), Shu-Fang Zhang(张淑芳), Hai-Jun Luo(罗海军), Xing-Ming Long(龙兴明), Fang Wu(吴芳), Liang Fang(方亮), Da-Peng Wei(魏大鹏), Fan-Ming Meng(孟凡明), Bao-Shan Hu(胡宝山)
Chin. Phys. B . 2017, 26(10): 104402. **doi:** 10.1088/1674-1056/26/10/104402

Simultaneous reconstruction of temperature distribution and radiative properties in participating media using a hybrid LSQR–PSO algorithm

Niu Chun-Yang, Qi Hong, Huang Xing, Ruan Li-Ming, Wang Wei, Tan He-Ping
Chin. Phys. B . 2015, 24(11): 114401. **doi:** 10.1088/1674-1056/24/11/114401

Spectral enhancement of thermal radiation by laser fabricating grating structure on nickel surface

Liu Song, Liu Shi-Bing
Chin. Phys. B . 2015, 24(5): 054401. **doi:** 10.1088/1674-1056/24/5/054401

Near-field radiative heat transfer in mesoporous alumina

Li Jing, Feng Yan-Hui, Zhang Xin-Xin, Huang Cong-Liang, Wang Ge
Chin. Phys. B . 2015, 24(1): 014401. **doi:** 10.1088/1674-1056/24/1/014401

Reconstruction model for temperature and concentration profiles of soot and metal-oxide nanoparticles in a nanofluid fuel flame by using a CCD camera*

Guannan Liu(刘冠楠)[1,2] and Dong Liu(刘冬)[1,2,†]

[1] MIIT Key Laboratory of Thermal Control of Electronic Equipment, School of Energy and Power Engineering, Nanjing University of Science and Technology, Nanjing 210094, China
[2] Advanced Combustion Laboratory, School of Energy and Power Engineering, Nanjing University of Science and Technology, Nanjing 210094, China

(Received 9 October 2017; revised manuscript received 28 December 2017; published online 26 April 2018)

This paper presents a numerical study on the simultaneous reconstruction of temperature and volume fraction fields of soot and metal-oxide nanoparticles in an axisymmetric nanofluid fuel sooting flame based on the radiative energy images captured by a charge-coupled device (CCD) camera. The least squares QR decomposition method was introduced to deal with the reconstruction inverse problem. The effects of ray numbers and measurement errors on the reconstruction accuracy were investigated. It was found that the reconstruction accuracies for volume fraction fields of soot and metal-oxide nanoparticles were easily affected by the measurement errors for radiation intensity, whereas only the metal-oxide volume fraction field reconstruction was more sensitive to the measurement error for the volume fraction ratio of metal-oxide nanoparticles to soot. The results show that the temperature, soot volume fraction, and metal-oxide nanoparticles volume fraction fields can be simultaneously and accurately retrieved for exact and noisy data using a single CCD camera.

Keywords: simultaneous reconstruction, temperature distribution, soot and metal-oxide volume fraction, nanofluid fuel flame

PACS: 44.40.+a, 44.05.+e, 02.30.Zz **DOI:** 10.1088/1674-1056/27/5/054401

1. Introduction

As hydrocarbon fuel supplies are gradually diminishing and environmental pollution is getting worse, the need for new alternatives to conventional hydrocarbon fuels is increasingly imperative. Furthermore, the development of hypersonic vehicle propulsion systems and power microelectromechanical systems are largely dependent on the physical and thermal properties of liquid fuels. Nanofluid fuels are uniform and stable suspensions containing available nanoscale additives in dilute concentrations (<1 vol.%),[1,2] which can enhance fuel energy density,[3,4] shorten ignition delay time,[5,6] improve reaction rates,[7,8] and reduce pollutant emissions.[9,10] In addition, many studies have shown that the addition of nanoparticles can promote the heat transfer rate of the base fuel.[11–16] Therefore, nanofluid fuels are expected to be the next generation of new fuels.

Sabourin *et al.*[7] compared the combustion of the monopropellant nitromethane with that of nitromethane containing colloidal particles of functionalized graphene sheets or metal hydroxides at room temperature and high-pressure conditions in a silica glass tube. The results demonstrate that the ignition temperature decreases and the burning rates increase for the suspensions compared to those of the monopropellant alone, especially in the burning rate improvement of greater than 175% for graphene sheet suspension. Gan *et al.*[17,18] investigated the burning characteristics of fuel droplets containing nanosized aluminum, boron, and iron particles, and they proposed various combustion stages (preheating, ignition, classical combustion, microexplosion, surfactant flame, and particle droplet combustion) through observing the recorded burning images of the nanofluid fuel droplets. Tanvir *et al.*[19] utilized a droplet stream flame to measure the burning rate of ethanol droplets with the addition of graphite nanoparticles, which was determined by estimating droplet sizes at corresponding locations via backlight shadowgraphy using a high-speed camera. Liu *et al.*[20] analyzed the geometrical parameters of nanofluid fuel flames using an image processing technique to study the combustion characteristics of flowing nanofluid fuels in a half-opening slot tube.

To date, studies on the combustion characteristics of nanofluid fuels are still in the primary stage and the combustion diagnostic methods for nanofluid fuels remain very limited. Temperature, volume fraction fields of soot, and metal-oxide nanoparticles in nanofluid fuel flame are important combustion characteristic parameters and should be measured accurately in the burning process of nanofluid fuel for the in-depth study.

The temperature and particle volume fraction measure-

*Project supported by the National Natural Science Foundation of China (Grant No. 51576100) and the Project of "Six Talent Summit" of Jiangsu Province, China (Grant No. 2014-XNY-002).

†Corresponding author. E-mail: dongliu@njust.edu.cn

© 2018 Chinese Physical Society and IOP Publishing Ltd

ment methods of the participating media are categorized as contact and noncontact diagnostic methods. The thermocouple method is one of the most common contact methods. Gan *et al.*[17] used a type-K thermocouple to suspend the nanofluid fuel droplet and measure its temperature history during the burning process. However, the nanoparticles in the droplet flame easily aggregate and deposit on the thermocouple surface, which decreases the accuracy and sensitivity of temperature measurement. Additionally, only the temperature of the single point in contact with the thermocouple tip can be measured.

Optical measurement techniques are currently preferred for their noncontact and multidimensional measurement advantages, which include tomography reconstruction, light extinction/scattering, and laser-induced incandescence (LII). Because a high-quality background radiation source is needed for transmission measurements, self-emission tomography systems have received particular attention in the last decade. The inverse analysis of radiative heat transfer based on a self-emission tomography system can be used to reconstruct the temperature, soot volume fraction, and radiation property fields of flame from the knowledge of the exit radiation intensity at the boundary surfaces. These days, the optical diagnostic technology combined with inverse radiation analysis for retrieving combustion characteristic fields of flame is developing fast and intensively.[21–43] Zhou *et al.*[21] first simulated the three-dimensional (3D) temperature distributions in furnaces through radiative energy images captured by multiple charge-coupled device (CCD) cameras mounted around the furnace. They proposed a fast algorithm based on the Monte Carlo method and angular factor effective of image formation to calculate the radiative energy, and used a modified Tikhonov regularization method to solve the inversion problem of 3D temperature distributions. Brisley *et al.*[23] and Lu *et al.*[25] applied an imaging-based multicolor pyrometric system combined with a novel optical splitting/filtering device to visualize temperature distributions in a coal-fired flame. Liu *et al.*[32] developed an inverse radiation analysis based on backward Monte Carlo (BMC) methods and the least squares QR (LSQR) algorithm for concurrent reconstruction of a temperature field and radiative properties in a two-dimensional (2D) rectangular, absorbing, emitting, and scattering gray medium by means of CCD cameras. Subsequently, Liu *et al.*[33,34] utilized multiple CCD cameras to retrieve the soot temperature and volume fraction profiles in a 3D optically thin flame. Niu *et al.*[38,39] developed hybrid LSQR-particle swarm optimization (LSQR-PSO) and LSQR-stochastic particle swarm optimization (LSQR-SPSO) algorithms to simultaneously reconstruct 3D temperature distribution and radiative properties of participating media. They found that the temperature field could be estimated to be more accurate than the absorption coefficients and the reconstruction accuracy of temperature distributions, scattering coefficients, and absorption coefficients decrease with the increase in extinction coefficient, but varies little with the scattering albedo. Ni *et al.*[40] used four CCD cameras combined with liquid crystal tunable filters (LCTF) to capture multispectral flame images for obtaining the line-of-sight radiation intensities, from which temperature and soot volume fraction profiles could be determined. The results show that the average error of the reconstructed volume fraction can be decreased from 8% by a two-color method to 3.17% through a multiwavelength method. Xu *et al.*[43] proposed a novel optical sectioning tomography for the measurement of 3D temperature of a flame through a single camera in combination with an ionic electrowetting-based variable-focus liquid lens.

The optical reconstruction methods mentioned above only focused on soot-involved flames, but the method for nanofluid fuel flame, in which metal-oxide nanoparticles and soot simultaneously exist, was insufficient. Niu *et al.*[44] and Huang *et al.*[45] developed a generalized sourced multiflux method (GSMFM) to simulate outgoing radiation intensities in arbitrary directions for describing the direct problem and used hybrid algorithms to reconstruct 3D temperature distribution and radiative properties in Al_2O_3 nanoparticle-filled ethylene diffusion flame. However, the retrieved estimations were the corresponding average values in the discrete element of the participating media, and the characteristic parameters for soot and metal-oxide nanoparticles were not distinguished reasonably. In order to further study nanofluid fuel flame, the characteristic parameters fields of metal-oxide nanoparticles and soot required to be respectively constructed.

In the present study, we develop a method for the simultaneous reconstruction of temperature and volume fraction fields of soot and metal-oxide nanoparticles in an axisymmetric nanofluid fuel sooting flame based on the radiative energy images captured by a single CCD camera. The CCD camera can instantaneously capture the images of the entire flame surface from which the radiative intensities can be obtained to overcome the difficulties in measuring the transient spectra of the entire flame by the spectrometer.

The contents of the paper are organized in the following way. The details of direct and inverse problems are described in Section 2. The direct problem for solving the radiation intensities was calculated directly using the line-of-sight discrete equation of the ray-tracing from ring to ring based on the assumed temperature, soot volume fraction, and metal-oxide volume fraction, while the inverse problem was formulated as a linear optimization problem which was solved by the LSQR method. In Section 3, the assumed temperature, volume fraction fields of soot and metal-oxide nanoparticles were provided for validating the method presented in Section 2. Some

results and discussion of the effects of ray number and measurement errors on reconstruction accuracy are given. Finally, the conclusions are presented in Section 4.

2. Analysis

2.1. Direct problem

The direct problem here was to calculate the exit line-of-sight radiation intensity emission based on the known temperature, soot volume fraction, and metal-oxide nanoparticle volume fraction fields in an axisymmetric nanofluid fuel sooting flame.

The considered system based on line-of-sight method is depicted in Fig. 1, which is similar to the system in Refs. [46] and [47]. The horizontal cross-section of the flame at a given height was divided into M rings with equal spacing, and the outer radius of each ring was represented by r. A CCD camera was used to capture flame cross-section image and the camera central wavelengths of the red channel (0.70 μm) and green channel (0.53 μm) were considered. The distance of the camera to the flame center was Le and the camera field angle was 2θ. The image pixel intensities were processed to obtain monochromatic radiation intensity emissions of the flame. N was assumed to be the number of the discrete radiation emission lines (ray number) received by the camera within the field angle.

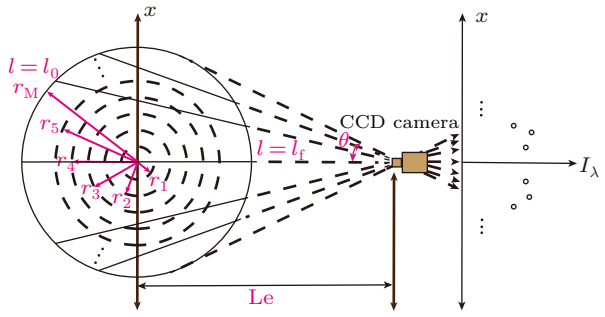


Fig. 1. (color online) Schematic of line-of-sight radiation intensities received by a CCD camera at a cross-section of a nanofluid fuel sooting flame.

The nanofluid fuel flame was assumed to be optically thin and the sizes of soot and metal-oxide nanoparticles in the flame were considered to be small in the Rayleigh scattering range. Therefore, the effects of flame species internal self-absorption and scattering can be negligible. The temperature fields of soot and metal-oxide nanoparticles here were considered to be equal and the particle system was independent scattering. Therefore, the following equation can be applied to the radiation intensity emission along ray j from the flame to the CCD camera,

$$I_\lambda(j) = \int_{l_0(j)}^{l_f(j)} [\kappa_\lambda(l) I_{b,\lambda}(l)]\,\mathrm{d}l = \sum_{i=1}^{M} \kappa_\lambda(i) I_{b,\lambda}(i) l_j(i) = \sum_{i=1}^{M} H_\lambda(i) l_j(i), \tag{1}$$

where $I_\lambda(j)$ is the monochromatic radiation emission intensity of flame into the spectrometer along the ray j, $\kappa_\lambda(l)$ is the local monochromatic absorption coefficient, $I_{b,\lambda}(l)$ is the local monochromatic radiation intensity of blackbody, $\kappa_\lambda(i)$ is the local monochromatic absorption coefficient in the ith ring, $I_{b,\lambda}(i)$ is the local monochromatic radiation intensity of a blackbody in the ith ring, $l_j(i)$ is the crossing length of the ray $j$in the ith ring, M is the total number of rings, and $H_\lambda(i)$ is the local monochromatic emission source in the ith ring, which is equal to $\kappa_\lambda(i)$ multiplied by $I_{b,\lambda}(i)$.

According to Wien's law

$$I_{b,\lambda}(i) = \frac{c_1}{\lambda^5 \pi \exp\left(\dfrac{c_2}{\lambda T(i)}\right)}, \tag{2}$$

where $T(i)$ is the temperature in the ith ring, and c_1 and c_2 are the first and second radiation constants.

The local monochromatic absorption coefficient $\kappa_\lambda(i)$ for a cloud of small particles in the independent scattering system can be calculated by the algebraic sum of the monochromatic absorption coefficient of every single particle in the corresponding ring[48]

$$\kappa_\lambda(i) = \sum_{w=1}^{U} N_{T,w} C_{\lambda,w} = \frac{\pi}{4} \sum_{w=1}^{U} D_w^2 N_{T,w} Q_{\lambda,w} = 1.5 \sum_{w=1}^{U} Q_{\lambda,w} \frac{f_{v,w}}{D_w}, \tag{3}$$

where U is the total number of particles in the ith ring, $N_{T,w}$ is the number of particles per unit volume, $C_{\lambda,w}$ is the absorption cross-section, D_w is the diameter of the wth single particle, $f_{v,w}$ is the volume fraction of the wth particle and $f_{v,w} = \pi D_w N_{T,w}/6$, where $Q_{\lambda,w}$ is the absorption factor of the wth single particle, which is given by the Rayleigh approximation as follows:

$$Q_{\lambda,w} = \frac{\pi D_w}{\lambda} \frac{24 n_\lambda k_\lambda}{(n_\lambda^2 - k_\lambda^2 + 2)^2 + 4 n_\lambda^2 k_\lambda^2}, \tag{4}$$

where n_λ and k_λ are the real and imaginary parts of the wavelength-dependent particle complex refraction index. The complex refraction indexes of metal-oxide nanoparticles and soot in this study were chosen from Refs. [49] and [50], respectively.

Substituting Eq. (4) into Eq. (3), $\kappa_\lambda(i)$ can be described as

$$\kappa_\lambda(i) = 1.5 \sum_{w=1}^{U} \frac{\pi}{\lambda} \frac{24 n_\lambda k_\lambda}{\left(n_\lambda^2 - k_\lambda^2 + 2\right)^2 + 4 n_\lambda^2 k_\lambda^2} f_{v,w}$$

$$= 1.5\frac{\pi}{\lambda}\left(\frac{24n_{\lambda,\text{soot}}k_{\lambda,\text{soot}}}{(n^2_{\lambda,\text{soot}}-k^2_{\lambda,\text{soot}}+2)^2+4n^2_{\lambda,\text{soot}}k^2_{\lambda,\text{soot}}}f_{\text{v,soot}} + \frac{24n_{\lambda,\text{NPs}}k_{\lambda,\text{NPs}}}{\left(n^2_{\lambda,\text{NPs}}-k^2_{\lambda,\text{NPs}}+2\right)^2+4n^2_{\lambda,\text{NPs}}k^2_{\lambda,\text{NPs}}}f_{\text{v,NPs}}\right), \quad (5)$$

where the subscript NPs refer to the metal-oxide nanoparticles.

Equation (1) can be discrete and expressed as

$$\begin{cases} I_\lambda(1) = \sum_{i=1}^{M}\kappa_\lambda(i)I_{\text{b},\lambda}(i)l_1(i) = \sum_{i=1}^{M}H_\lambda(i)l_1(i), \\ \vdots \\ I_\lambda(j) = \sum_{i=1}^{M}\kappa_\lambda(i)I_{\text{b},\lambda}(i)l_j(i) = \sum_{i=1}^{M}H_\lambda(i)l_j(i), \\ \vdots \\ I_\lambda(N) = \sum_{i=1}^{M}\kappa_\lambda(i)I_{\text{b},\lambda}(i)l_N(i) = \sum_{i=1}^{M}H_\lambda(i)l_N(i). \end{cases} \quad (6)$$

Then, equation (6) can be transformed into a matrix form as

$$\boldsymbol{I}_\lambda = \boldsymbol{L}\cdot\boldsymbol{H}_\lambda \quad (7)$$

where $\boldsymbol{I}_\lambda$ is the vector of monochromatic radiation intensities of the flame ($\boldsymbol{I}_\lambda \in R^N$), $\boldsymbol{L}$ is the matrix of the crossing length in each ring for each ray ($\boldsymbol{L} \in R^{N\times M}$), and $\boldsymbol{H}_\lambda$ is the vector of local monochromatic emission source ($\boldsymbol{H}_\lambda \in R^M$).

The monochromatic emission source $\boldsymbol{H}_\lambda$ can be obtained from Eqs. (2) and (5) with the known temperature, volume fraction distributions of soot, and metal-oxide nanoparticles. Then, equation (7) was used to calculate radiation intensity $\boldsymbol{I}_\lambda$.

2.2. Inverse problem

For the inverse problem, the temperature, volume fraction fields of soot, and metal-oxide nanoparticles were assumed to be unknown. These parameters can be estimated by the exit line-of-sight radiation intensity vector $\boldsymbol{I}_\lambda$ measured by a single CCD camera using the inverse method.

Here, the LSQR algorithm was introduced for solving Eq. (7) to obtain the value of $\boldsymbol{H}_\lambda$ from the measured radiation intensity vector $\boldsymbol{I}_\lambda$. The details of the LSQR method are available in Refs. [51]–[53] and the method was successfully used to solve the inverse problem in Refs. [30], [32], [33], [36], [38], and [39]. Another parameter Rt was introduced to represent the volume fraction ratio of metal-oxide nanoparticles to soot, i.e., $\text{Rt} = f_{\text{v,NPs}}/f_{\text{v,soot}}$. The volume fraction of particles in any particular (organic or inorganic) system can be determined by thermophoretic sampling particle diagnostic (TSPD) technique via measuring the particle mass deposited on an electron microscope grid during a certain sampling time.[54] When using the TSPD method, copper grids for the transmission electron microscope (TEM) measurements were treated as the sampling probes in the nanofluid fuel flame, and a very short sampling time was chosen to prevent overlapping of the particle aggregates. The local soot and metal-oxide nanoparticles volume fractions in flame were respectively expressed as[55,56]

$$f_{\text{v,soot}} = \frac{2R_xV_{\text{p,soot}}}{D_\text{T}\text{Nu}_xA_it_\text{e}}\left[1-\left(\frac{T_\text{w}}{T_\text{g}}\right)^2\right]^{-1}, \quad (8)$$

$$f_{\text{v,NPs}} = \frac{2R_xV_{\text{p,NPs}}}{D_\text{T}\text{Nu}_xA_it_\text{e}}\left[1-\left(\frac{T_\text{w}}{T_\text{g}}\right)^2\right]^{-1}, \quad (9)$$

where R_x is the vertical position on the sampling probe, $V_{\text{p,soot}}$ is the soot total volume deposited in a TEM image, $V_{\text{p,NPs}}$ is the total volume of metal-oxide nanoparticles deposited in a TEM image, D_T is the particle thermophoretic diffusivity, Nu_x is the local Nusselt number for heat transfer, A_i is the total area of the TEM image, t_w is the sampling time, and T_w and T_g are the thermophoretic probe wall temperature and gas temperature, respectively.

According to Eqs. (8) and (9), the volume fraction ratio of metal-oxide nanoparticles to soot was simplified to

$$\text{Rt} = \frac{f_{\text{v,NPs}}}{f_{\text{v,soot}}} = \frac{V_{\text{p,NPs}}}{V_{\text{p,soot}}}, \quad (10)$$

where $V_{\text{p,NPs}}$ and $V_{\text{p,soot}}$ were given by TEM analysis followed by the image processing technique. Therefore, from Eq. (10), Rt can be obtained without needing to know the gas temperature at the corresponding location in the flame.

After H_λ at two wavelengths was retrieved and Rt was measured, the local temperature, soot volume fraction, and metal-oxide nanoparticle volume fraction can be finally calculated by

$$T(i) = \frac{c_2\left(\frac{1}{\lambda_2}-\frac{1}{\lambda_1}\right)}{\ln\frac{H_{\lambda_1}(i)}{H_{\lambda_2}(i)} - \ln S + 5\ln\frac{\lambda_1}{\lambda_2}}, \quad (11)$$

$$S = \frac{\frac{n_{\lambda_{1,\text{soot}}}k_{\lambda_{1,\text{soot}}}}{\left(n^2_{\lambda_{1,\text{soot}}}-k^2_{\lambda_{1,\text{soot}}}+2\right)^2+4n^2_{\lambda_{1,\text{soot}}}k^2_{\lambda_{1,\text{soot}}}}\frac{1}{\lambda_1} + \frac{n_{\lambda_{1,\text{NPs}}}k_{\lambda_{1,\text{NPs}}}}{\left(n^2_{\lambda_{1,\text{NPs}}}-k^2_{\lambda_{1,\text{NPs}}}+2\right)^2+4n^2_{\lambda_{1,\text{NPs}}}k^2_{\lambda_{1,\text{NPs}}}}\frac{\text{Rt}}{\lambda_1}}{\frac{n_{\lambda_{2,\text{soot}}}k_{\lambda_{2,\text{soot}}}}{\left(n^2_{\lambda_{2,\text{soot}}}-k^2_{\lambda_{2,\text{soot}}}+2\right)^2+4n^2_{\lambda_{2,\text{soot}}}k^2_{\lambda_{2,\text{soot}}}}\frac{1}{\lambda_2} + \frac{n_{\lambda_{2,\text{NPs}}}k_{\lambda_{2,\text{NPs}}}}{\left(n^2_{\lambda_{2,\text{NPs}}}-k^2_{\lambda_{2,\text{NPs}}}+2\right)^2+4n^2_{\lambda_{2,\text{NPs}}}k^2_{\lambda_{2,\text{NPs}}}}\frac{\text{Rt}}{\lambda_2}}, \quad f_{\text{v,soot}}(i) = \frac{H_{\lambda_1}(i)}{36\pi I_{\text{b}\lambda_1}(i)(\text{SS})}, \quad (12)$$

$$\mathrm{SS} = \frac{n_{\lambda_{1,\mathrm{soot}}} k_{\lambda_{1,\mathrm{soot}}}}{\left(n^2_{\lambda_{1,\mathrm{soot}}} - k^2_{\lambda_{1,\mathrm{soot}}} + 2\right)^2 + 4n^2_{\lambda_{1,\mathrm{soot}}} k^2_{\lambda_{1,\mathrm{soot}}}} \frac{1}{\lambda_1} + \frac{n_{\lambda_{1,\mathrm{NPs}}} k_{\lambda_{1,\mathrm{NPs}}}}{\left(n^2_{\lambda_{1,\mathrm{NPs}}} - k^2_{\lambda_{1,\mathrm{NPs}}} + 2\right)^2 + 4n^2_{\lambda_{1,\mathrm{NPs}}} k^2_{\lambda_{1,\mathrm{NPs}}}} \frac{\mathrm{Rt}}{\lambda_1},$$
$$f_{\mathrm{v,NPs}}(i) = \mathrm{Rt}(i) f_{\mathrm{v,soot}}(i). \quad (13)$$

The inverse procedure for retrieving temperature and volume fraction distributions of soot and metal-oxide nanoparticles using a single CCD camera can be summarized as follows.

Step 1 According to the geometrical relationships between rings and rays, the crossing length matrix $\boldsymbol{L}$ was calculated.

Step 2 Based on the calculated matrix $\boldsymbol{L}$ and the measured radiation intensity vectors $\boldsymbol{I}_{\lambda 1}$ and $\boldsymbol{I}_{\lambda 2}$ by the CCD camera, local monochromatic emission sources $\boldsymbol{H}_{\lambda 1}$ and $\boldsymbol{H}_{\lambda 2}$ in Eq. (7) at two wavelengths can be respectively solved via the LSQR method.

Step 3 Obtain the volume fraction ratio vector **Rt** by the TSPD technique.

Step 4 Compute the unknown temperature and volume fraction distributions of soot and metal-oxide nanoparticles according to the formulations described in Eqs. (11)–(13).

3. Results and discussion

The radiation intensities vectors $\boldsymbol{I}_\lambda$ received by the CCD camera were simulated by adding random errors of normal distribution ξ_1 with zero average value μ_1 and mean square deviation σ_1 to the exact intensities obtained from the direct problem. Meanwhile, the measured volume fraction ratio vector **Rt** obtained from the TSPD techniques were simulated by adding random errors of normal distribution ξ_2 with zero average value μ_2 and mean square deviation σ_2 to the exact volume fraction ratio vector.

$$\boldsymbol{I}_{\lambda,\mathrm{meas}} = (\mu_1 + \sigma_1 \xi_1)\boldsymbol{I}_{\lambda,\mathrm{exa}} + \boldsymbol{I}_{\lambda,\mathrm{exa}}, \quad (14)$$
$$\mathbf{Rt}_{\mathrm{meas}} = (\mu_2 + \sigma_2 \xi_2)\mathrm{Rt}_{\mathrm{exa}} + \mathbf{Rt}_{\mathrm{exa}}, \quad (15)$$

where $\boldsymbol{I}_{\lambda,\mathrm{meas}}$ and $\boldsymbol{I}_{\lambda,\mathrm{exa}}$ are the measured radiation intensity vector with error and the exact radiation intensity vector. $\mathbf{Rt}_{\mathrm{meas}}$ and $\mathbf{Rt}_{\mathrm{exa}}$ are the measured volume fraction ratio vector with error and the exact volume fraction ratio vector. The signal-to-noise ratio (SNR) is defined in terms of the logarithmic decibel scale.[31] SNR of $\boldsymbol{I}_{\lambda,\mathrm{meas}}$ and $\mathbf{Rt}_{\mathrm{meas}}$ are described, respectively, as

$$\mathrm{SNR}_1 = 20\log\left(\left[\frac{1}{N}\sum_{j=1}^{N}\sigma_1^2\xi_{1j}^2\right]^{-1/2}\right), \quad j = 1,2,\ldots,N, \quad (16)$$

$$\mathrm{SNR}_2 = 20\log\left(\left[\frac{1}{M}\sum_{i=1}^{M}\sigma_2^2\xi_{2i}^2\right]^{-1/2}\right), \quad i = 1,2,\ldots,M, \quad (17)$$

where SNR_1 and SNR_2 are the measured SNR of radiation intensity and volume fraction ratio.

To demonstrate the validity and robustness of the reconstruction method, the distributions of temperature and soot volume fraction based on the laminar ethylene diffusion flame at 30 mm in Ref. [20] and the metal-oxide nanoparticles volume fraction distribution estimated from the diffusion flame of ethanol-based fuel with the addition of Al_2O_3 nanoparticles at 0.05 wt% concentration were adopted in the following simulation research. The flame radius at the given height was set as 3 mm and the horizontal cross-section was evenly divided into 30 rings with equal spacing of 0.1 mm. Figure 2 shows the exact temperature, volume fraction profiles of soot and metal-oxide nanoparticles. The field angle of the CCD camera was assumed to be 80° and the distance of the CCD to the flame center Le was calculated to be 4.7 mm.

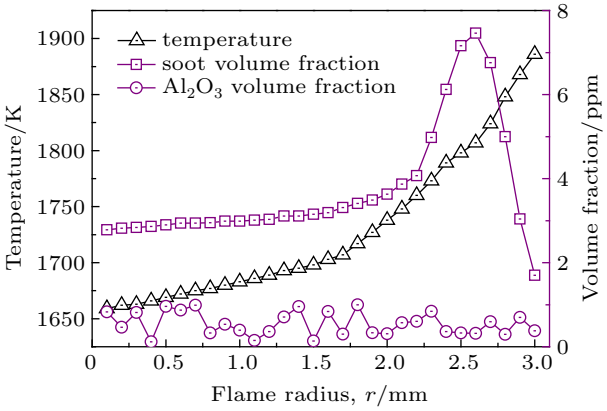


Fig. 2. (color online) Exact temperature, Al_2O_3 nanoparticles volume fraction, and soot volume fraction fields.

The relative errors for temperature ($E_{T,\mathrm{rel}}$), soot volume fraction ($E_{f_{\mathrm{v,soot,rel}}}$), and Al_2O_3 volume fraction ($E_{f_{\mathrm{v},Al_2O_3,\mathrm{rel}}}$) reconstruction in each ring are defined as

$$E_{T,\mathrm{rel}}(i) = 100\frac{|T_{\mathrm{rec}}(i) - T_{\mathrm{exa}}(i)|}{T_{\mathrm{exa}}(i)}, \quad (18)$$
$$E_{f_{\mathrm{v,soot,rel}}}(i) = 100\frac{|f_{\mathrm{v,soot,rec}}(i) - f_{\mathrm{v,soot,exa}}(i)|}{f_{\mathrm{v,soot,exa}}(i)}, \quad (19)$$
$$E_{f_{\mathrm{v},Al_2O_3,\mathrm{rel}}}(i) = 100\frac{|f_{\mathrm{v},Al_2O_3,\mathrm{rec}}(i) - f_{\mathrm{v},Al_2O_3,\mathrm{exa}}(i)|}{f_{\mathrm{v},Al_2O_3,\mathrm{exa}}(i)}, \quad (20)$$

where T_{rec} and T_{exa} represent the reconstructed and exact temperature, $f_{\mathrm{v,soot,rec}}$ and $f_{\mathrm{v,soot,exa}}$ represent the reconstructed and exact soot volume fraction, $f_{\mathrm{v},Al_2O_3,\mathrm{rec}}$ and $f_{\mathrm{v},Al_2O_3,\mathrm{exa}}$ represent the reconstructed and exact Al_2O_3 nanoparticles volume fraction, respectively.

In the following three cases, the effects of ray number, measurement errors of radiation intensity $\boldsymbol{I}_\lambda$ and volume fraction ratio **Rt** on the accuracies of reconstructed results were investigated. First, it was assumed that only $\boldsymbol{I}_\lambda$ had measurement error in case 1. Then, only **Rt** had measurement errors in case 2. Finally, both $\boldsymbol{I}_\lambda$ and **Rt** have measurement errors simultaneously in case 3.

3.1. Case 1

In this case, the effects of ray number and measurement errors for radiation intensity $\boldsymbol{I}_\lambda$ on the reconstruction accuracy and stability were examined.

3.1.1. Effects of ray number on reconstruction accuracy

The monochromatic radiation intensity emission profiles of the flame at the red channel (700 nm) and green channel (530 nm) using four ray numbers N (30, 60, 90, and 120) are presented in Fig. 3. Here, these different ray numbers N and three different SNR_1 (65 dB, 60 dB, 46 dB) were studied and compared, as shown in Fig. 4. It can be found that with the increase in ray number from 30 to 90, the average and maximum relative errors of temperature, soot volume fraction, and Al_2O_3 volume fraction distributions reconstruction decreased significantly under certain fixed measurement errors. However, from ray number 90 to 120, these relative errors did not decrease obviously, and the computing time increased. Therefore, ray number 90 was chosen as the best reconstructed result, which was the trade-off between the reconstruction accuracy and computing time. With $N = 90$ and $\mathrm{SNR}_1 = 46$ dB, the average relative errors of temperature and volume fraction distributions reconstruction of soot and Al_2O_3 are 0.12%, 1.19%, and 1.19%, respectively. The respective maximum relative errors for these parameters are 0.51%, 5.15%, and 5.15%. The SNR of the CCD camera used in the experiments is usually higher than 65 dB, which means that better reconstructed results could be expected. Moreover, the reconstructed results of temperature and volume fraction distributions with $\mathrm{SNR}_1 = 46$ dB are displayed in Fig. 5. In general, the reconstructed fields agreed well with the exact values, especially at the locations with high temperature range from 1738 K to 1886 K. However, the reconstructed results at locations with low temperatures were easily influenced by measurement errors, because less radiative information from these locations could be received by the CCD camera.

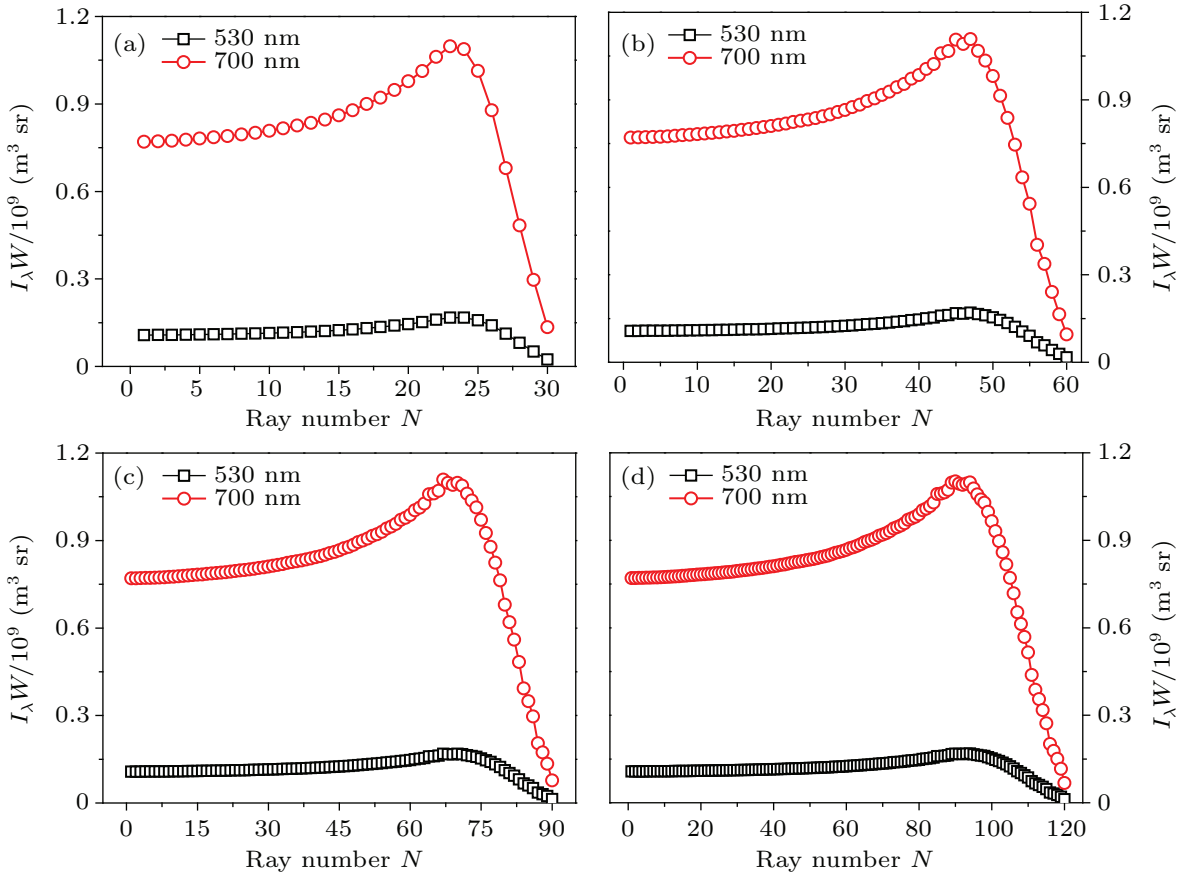


Fig. 3. (color online) Monochromatic radiation intensity emission I_λ profiles of the flame at the red channel (700 nm) and the green channel (530 nm) using ray number ((a) 30, (b) 60, (c) 90, and (d) 120).

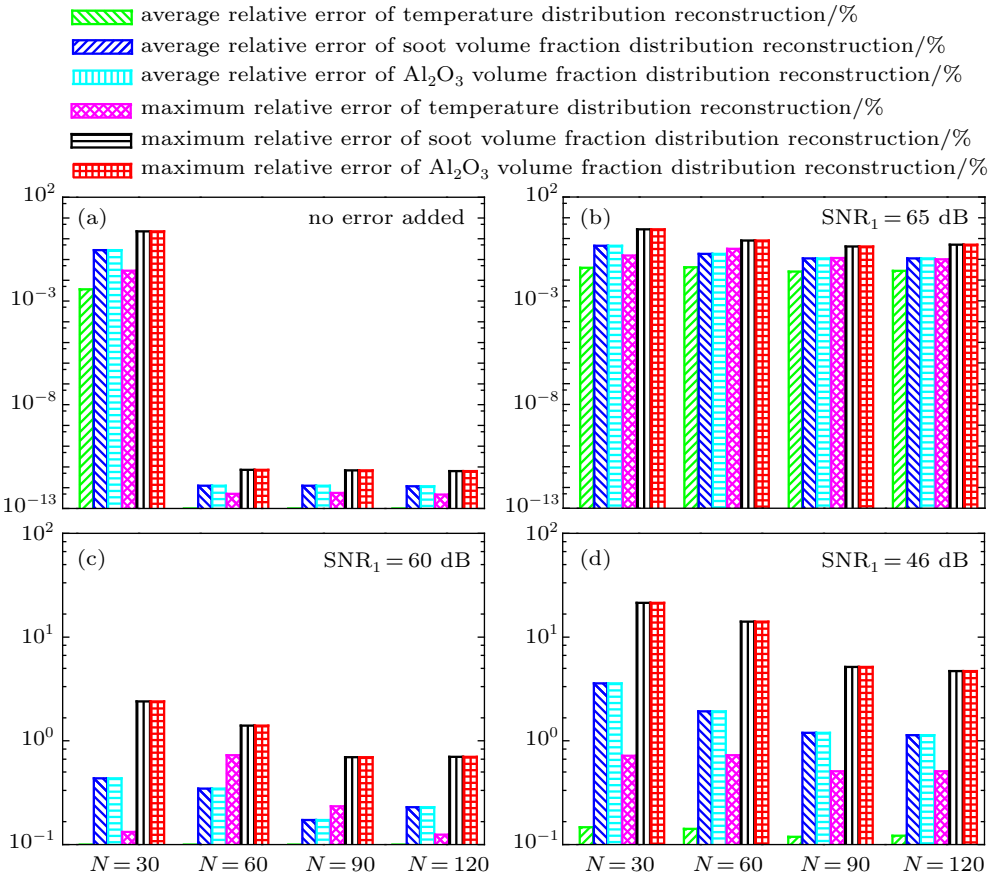


Fig. 4. (color online) Effects of ray numbers (N) and measurement errors for radiation intensity I_λ (SNR_1) on the reconstruction accuracy. (a) No error added, (b) $SNR_1 = 65$ dB, (c) $SNR_1 = 60$ dB, (d) $SNR_1 = 46$ dB.

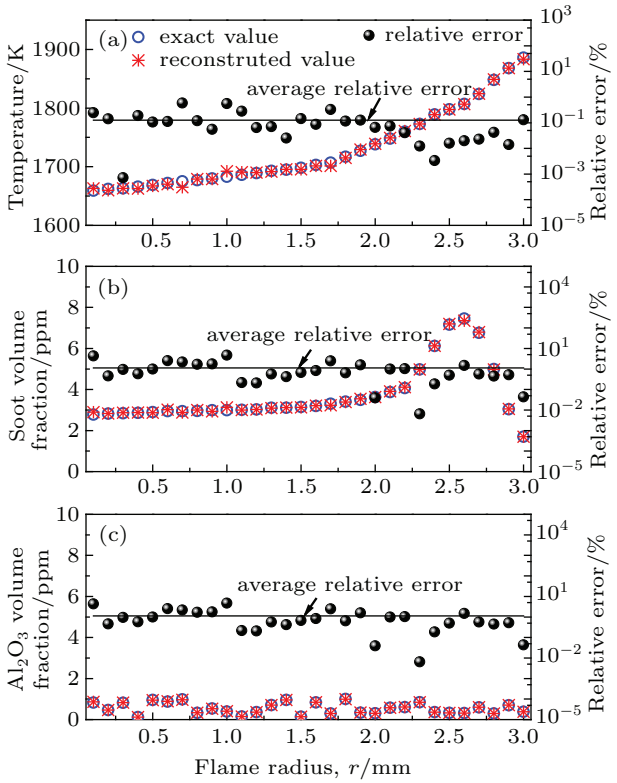


Fig. 5. (color online) (a) Local temperature and volume fraction distributions reconstruction of (b) soot and (c) Al_2O_3 nanoparticles using ray number 90 on the condition of measurement error for radiation intensity I_λ (SNR_1) of 46 dB. For the sake of comparison, the exact value and relative error are also included.

3.1.2. Effect of measurement error on stability of the reconstruction method

Here, ray number 90 was used and four different SNR_1 were assumed. Owing to the random errors adding to the exact solution of the direct problem, the stability of the reconstruction method was tested through 20 samples, as shown in Fig. 6. The average and maximum relative errors of volume fraction distribution reconstruction of Al_2O_3 stayed exactly the same as those of soot. The maximum of the maximum relative errors of the temperature distribution reconstruction for 20 samples were below 0.88%, even with SNR_1 as low as 46 dB. Therefore, the reconstruction results of the temperature field were satisfying under these measurement errors. When SNR_1 was 60 dB, the maximum of the maximum relative errors of volume fraction distribution reconstruction for 20 samples was below 1.79%. However, as SNR_1 further decreased to 46 dB, the maximum of the maximum relative errors of volume fraction distribution reconstruction for 20 samples increased to 14.24%, which meant that the reconstruction failed. If the temperature and volume fraction fields of soot and Al_2O_3 nanoparticles were desired to be reconstructed accurately, the SNR of the CCD camera should be limited within an appropriate range.

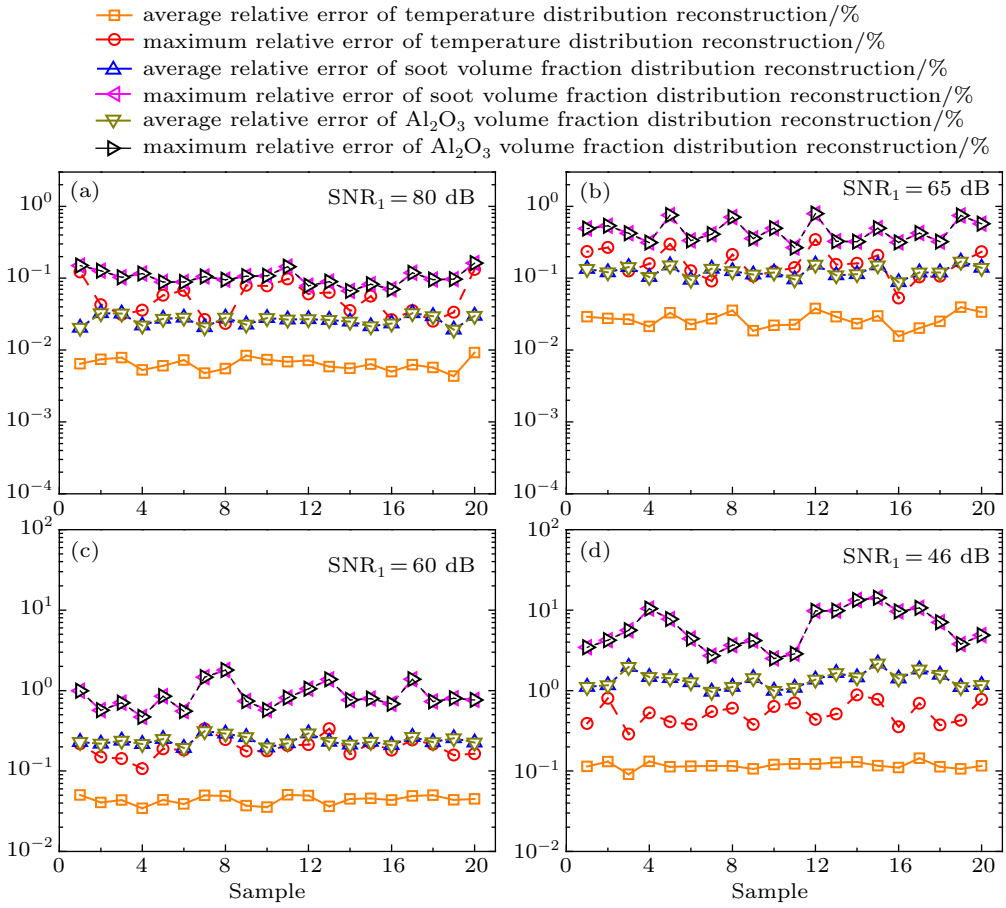


Fig. 6. (color online) Effects of measurement errors for radiation intensity $\boldsymbol{I}_\lambda$ (SNR_1) on the reconstruction accuracy with 20 samples. (a) $\mathrm{SNR}_1 = 80$ dB, (b) $\mathrm{SNR}_1 = 65$ dB, (c) $\mathrm{SNR}_1 = 60$ dB, (d) $\mathrm{SNR}_1 = 46$ dB

3.2. Case 2

In this case, the effects of measurement errors for the volume fraction ratio **Rt** on the reconstruction accuracy were examined. Four SNR_2 (65 dB, 60 dB, 46 dB, and 39 dB) were tested. Owing to the random errors adding to the exact volume fraction ratio **Rt**, all the reconstruction results were the average results of 20 samples.

The average of the local relative errors of temperature, soot volume fraction, and Al_2O_3 volume fraction reconstruction of 20 samples are shown in Fig. 7.

From Fig. 7, the local relative error of the temperature reconstruction maintained the lowest level, whereas that of the Al_2O_3 volume fraction reconstruction maintained the highest level. The Al_2O_3 volume fraction was calculated using the soot volume fraction multiplied by the measured volume fraction ratio. Therefore, when the volume fraction ratio had the measurement error, the reconstruction error of the Al_2O_3 volume fraction was larger than that of soot volume fraction. However, when the measurement of volume fraction ratio had no error, the relative reconstruction errors of Al_2O_3 nanoparticles volume fraction and soot volume fraction were the same. This implied that compared with the other reconstruction, the Al_2O_3 volume fraction distribution reconstruction was more susceptible to the measurement error of the volume fraction ratio **Rt**. When $\mathrm{SNR}_2 = 39$ dB, the maximum of local relative errors of Al_2O_3 volume fraction reconstruction was no more than 1.2% at the location with a flame radius of 2.1 mm. Therefore, the parameter distributions of the temperature and volume fractions can be accurately retrieved even when SNR_2 was as low as 39 dB, which decreased the requirement of the high measurement accuracy of the volume fraction ratio **Rt** by the TSPD technique.

3.3. Case 3

In this case, the measurement errors in the simultaneous presence of radiation intensity $\boldsymbol{I}_\lambda$ and volume fraction ratio **Rt** on the reconstruction accuracy are displayed in Fig. 8. All the reconstructed relative errors were the average results of 20 samples.

In comparison to the measurement error for the volume fraction ratio **Rt**, the reconstructed results were more easily influenced by that for the radiation intensity $\boldsymbol{I}_\lambda$. As SNR_2 decreased from 80 dB to 46 dB under $\mathrm{SNR}_1 = 46$ dB, the average relative errors of temperature and volume fraction distributions reconstruction of soot and Al_2O_3 increased by factors of 0.09,

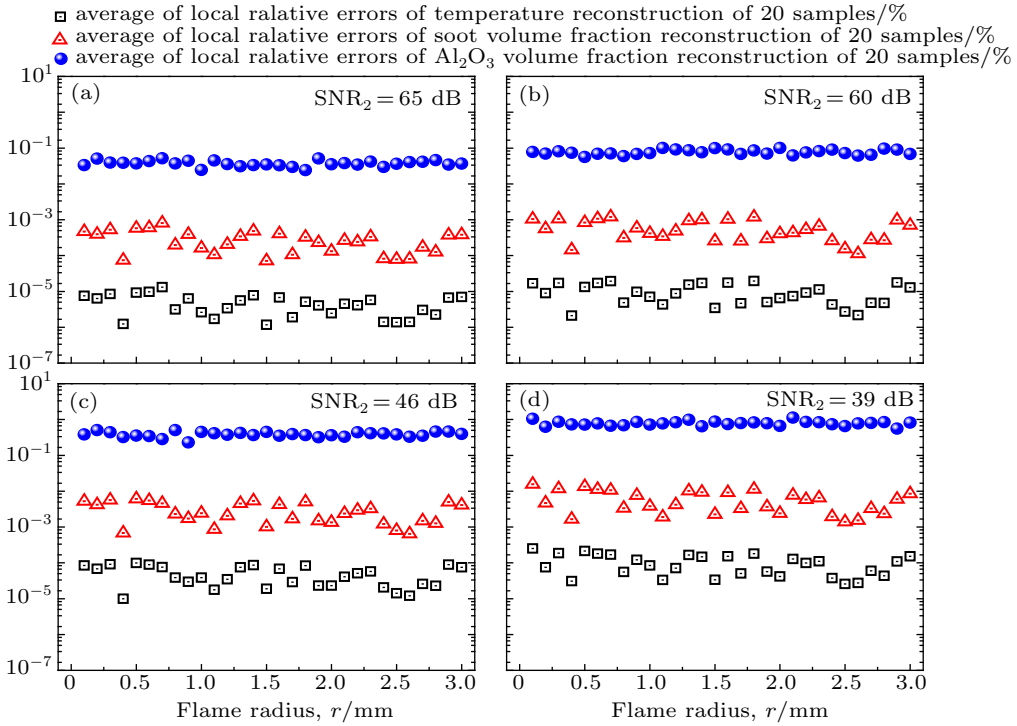


Fig. 7. (color online) Effects of measurement errors for volume fraction ratio **Rt** (SNR_2) on the reconstruction accuracy. (a) $SNR_2 = 65$ dB, (b) $SNR_2 = 60$ dB, (c) $SNR_2 = 46$ dB, (d) $SNR_2 = 39$ dB

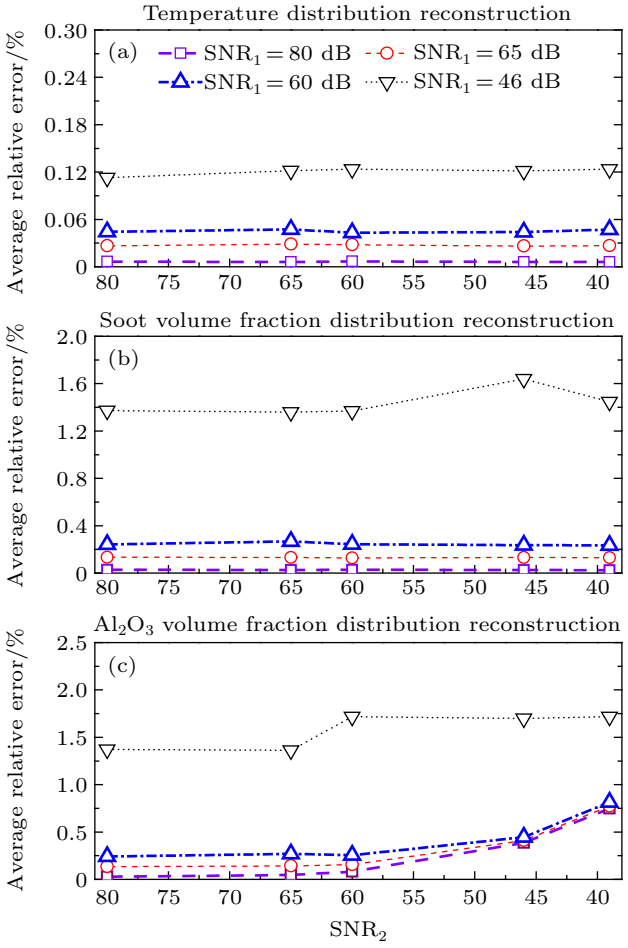


Fig. 8. (color online) Effects of measurement errors for radiation intensity I_λ (SNR_1) and volume fraction ratio **Rt** (SNR_2) on the reconstruction accuracy. (a) Temperature distribution reconstruction, (b) soot volume fraction distribution reconstruction, (c) Al_2O_3 volume fraction distribution reconstruction.

0.2, and 0.24, respectively. While SNR_1 decreased from 80 dB to 46 dB under $SNR_2 = 46$ dB, the respective average relative errors for these parameters increased by factors of 19, 53.67, and 3.36.

The reconstruction accuracies of the temperature and soot volume fraction distributions were not sensitive to the measurement error for the volume fraction ratio **Rt** and the variations in the average reconstructed relative errors for these parameters were almost unobservable with the decrease in SNR_2.

When $SNR_1 = 46$ dB and $SNR_2 = 39$ dB, the average relative error of the temperature distribution reconstruction was only 0.12%, and that of the volume fraction distribution reconstruction of soot and Al_2O_3 were only approximately 1.45% and 1.72%, respectively. Therefore, the reconstruction method developed in this study was effective and robust, and could reasonably retrieve the temperature and volume fraction fields of soot and metal-oxide nanoparticles in an axisymmetric nanofluid fuel sooting flame.

4. Conclusions

An efficient numerical inverse radiation analysis was proposed to reconstruct the temperature and volume fraction fields of soot and metal-oxide nanoparticles in an axisymmetric nanofluid fuel sooting flame using a single CCD camera. Numerical simulations were used and the reconstructed results were acceptable, even in the presence of simultaneous measurement errors of SNR_1 of radiation intensity I_λ as low as 46 dB and SNR_2 of volume fraction ratio **Rt** as low as

39 dB. The numeral analyses show that the method was capable and robust to concurrently retrieve the temperature and volume fraction fields of soot and metal-oxide nanoparticles in the nanofluid fuel flame for both exact and noisy data.

References

[1] Basu S and Miglani A 2016 *Int. J. Heat Mass Transf.* **96** 482
[2] Choi S U S 2009 *J. Heat Transfer* **131** 033106
[3] Jones M, Li C H, Afjeh A and Peterson G 2011 *Nanoscale Res. Lett.* **6** 246
[4] Wen D S 2010 *Energy Environ. Sci.* **3** 591
[5] Javed I, Baek S W and Waheed K 2015 *Combust. Flame* **162** 191
[6] Javed I, Baek S W and Waheed K 2015 *Combust. Flame* **162** 774
[7] Sabourin J L, Dabbs D M, Yetter R A, Dryer F L and Aksay I A 2009 *Acs Nano* **3** 3945
[8] Huang X F and Li S J 2016 *Fuel* **177** 113
[9] Selvan V A M, Anand R B and Udayakumar M 2014 *Fuel* **130** 160
[10] Sarvestany N S, Farzad A, Bajestan E E and Mir M 2014 *J. Dispers. Sci. Technol.* **35** 1745
[11] Xuan Y M, Li Q and Hu W 2003 *AICHE J.* **49** 1038
[12] Xuan Y M and Li Q 2003 *J. Heat Transf.* **125** 151
[13] Xuan Y M and Li Q 2000 *Int. J. Heat Fluid Flow* **21** 58
[14] Xing J J, Wu Z H, Xie H Q, Wang Y Y, Li Y H and Mao J H 2017 *Chin. Phys. B* **26** 104401
[15] Zhou X F and Gao L 2007 *Chin. Phys.* **16** 2028
[16] Hayat T, Imtiaz M, Alsaedi A and and Mansoor R 2014 *Chin. Phys. B* **23** 054701
[17] Gan Y N and Qiao L 2011 *Combust. Flame* **158** 354
[18] Gan Y N, Lim Y S and Qiao L 2012 *Combust. Flame* **159** 1732
[19] Tanvir S and Qiao L 2016 *Combust. Flame* **166** 34
[20] Liu G N and Liu D 2017 *Sci. China Technol. Sci.* **60** 1075
[21] Zhou H C, Han S D, Sheng F and Zheng C G 2002 *J. Quant. Spectrosc. Radiat. Transf.* **72** 361
[22] Snelling D R, Thomson K A, Smallwood G J, Gülder O L, Weckman E J and Fraser R A 2002 *AIAA J.* **40** 1789
[23] Brisley P M, Lu G, Yan Y and Cornwell S 2005 *IEEE Trans. Instrum. Meas.* **54** 1417
[24] Lou C and Zhou H C 2005 *Combust. Flame* **143** 97
[25] Lu G, Yan Y, Cornwell S and Riley G 2006 *Proc. IEEE* **55** 1658
[26] Lou C, Zhou H C, Yu P F and Jiang Z W 2007 *Proc. Combust. Inst.* **31** 2771
[27] Wang F, Liu D, Cen K F, Yan J H, Huang Q X and Chi Y 2008 *J. Quant. Spectrosc. Radiat. Transf.* **109** 2171
[28] Liu D, Wang F, Huang Q X, Yan J H, Chi Y and Cen K F 2008 *Chin. Phys. B* **17** 1312
[29] Liu D, Wang F, Huang Q X, Yan J H, Chi Y and Cen K F 2008 *Acta Phys. Sin.* **57** 4812 (in Chinese)
[30] Liu D, Wang F, Cen K F, Yan J H, Huang Q X and Chi Y 2008 *Opt. Lett.* **33** 422
[31] Huang Q X, Wang F, Liu D, Ma Z Y, Yan J H, Chi Y and Cen C F 2009 *Combust. Flame* **156** 565
[32] Liu D, Yan J H, Wang F, Huang Q X, Chi Y and Cen K F 2010 *Int. J. Heat Mass Transf.* **53** 4474
[33] Liu D, Huang Q X, Wang F, Chi Y, Cen K F and Yan J H 2010 *J. Heat Transfer* **132** 061202
[34] Yan J H, Wang F, Huang Q X, Chi Y, Cen K F and Liu D 2011 *Acta Phys. Sin.* **60** 060701 (in Chinese)
[35] Liu D, Yan J H and Cen K F 2011 *Int. J. Heat Mass Transf.* **54** 1684
[36] Liu D, Yan J H and Cen K F 2012 *Int. J. Heat Mass Transf.* **55** 1553
[37] Liu D, Yan J H, Wang F, Huang Q X, Chi Y and Cen K F 2012 *Fuel* **93** 397
[38] Niu C Y, Qi H, Huang X, Ruan L M, Wang W and Tan H P 2015 *Chin. Phys. B* **24** 114401
[39] Niu C Y, Qi H, Lew Z Y, Ruan L M and Tan H P 2015 3*nd International Workshop on Heat Transfer Advances for Energy Conservation and Pollution Control*, October 16–19, Taipei, Taiwan, China
[40] Ni M J, Zhang H D, Wang F, Xie Z C, Huang Q X, Yan J H and Cen K F 2016 *Appl. Therm. Eng.* **96** 421
[41] Sun J, Xu C L, Zhang B, Wang S M, Hossain M M, Qi H and Tan H P 2016 *Instrum. Meas. Technol. Conf. Proc*. 1–6
[42] Liu D 2016 *Therm. Sci.* **20** 493
[43] Xu C L, Zhao W C, Hu J H, Zhang B and Wang S M 2017 *Fuel* **196** 550
[44] Niu C Y, Qi H, Huang X, Ruan L M and Tan H P 2016 *J. Quant. Spectrosc. Radiat. Transf.* **184** 44
[45] Huang X, Qi H, Niu C Y, Ruan L M, Tan H P, Sun J and Xu C L 2017 *Appl. Therm. Eng.* **115** 1337
[46] Zhou H C, Luo C and Lu J 2008 *The 6th International Symposium on Measurement Techniques for Multiphase Flows*, December 15–17, 2008, Okinawa, Japan, p. 012086
[47] Yan W J, Zheng S and Zhou H C 2017 *Appl. Therm. Eng.* **124** 1014
[48] Modest M F 2003 *Radiative Heat Transfer,* 2nd edn. (America: Academic Press) pp. 361–412
[49] Querry M R 1985 *Optical Constants* p. 12
[50] Chang H and Charalampopoulos T T 1990 *Proc. R. Soc. A* **430** 577
[51] Lanczons C 1950 *J. Res. Natl. Bur. Stand.* **45** 255
[52] Paige C C and Saunders M A 1982 *AMC Trans. Math. Softw.* **8** 43
[53] Paige C C and Saunders M A 1982 *AMC Trans. Math. Softw.* **8** 195
[54] Köylü Ü Ö, McEnally C S, Rosner D E and Pfefferle L D 1997 *Combust. Flame* **110** 494
[55] Xu Z W, Zhao H B, Chen X B and Lou C 2017 *Combust. Flame* **180** 158
[56] Xu Z W and Zhao H B 2015 *Combust. Flame* **162** 2200